Faraday Discussions

Accepted Manuscript

This manuscript will be presented and discussed at a forthcoming Faraday Discussion meeting. All delegates can contribute to the discussion which will be included in the final volume.

Register now to attend! Full details of all upcoming meetings: http://rsc.li/fd-upcoming-meetings

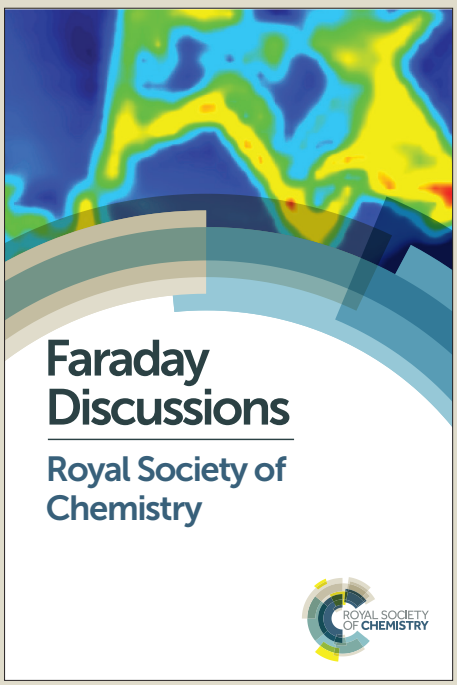

This is an *Accepted Manuscript*, which has been through the Royal Society of Chemistry peer review process and has been accepted for publication.

Accepted Manuscripts are published online shortly after acceptance, before technical editing, formatting and proof reading. Using this free service, authors can make their results available to the community, in citable form, before we publish the edited article. We will replace this *Accepted Manuscript* with the edited and formatted *Advance Article* as soon as it is available.

You can find more information about *Accepted Manuscripts* in the Information for Authors.

Please note that technical editing may introduce minor changes to the text and/or graphics, which may alter content. The journal's standard Terms & Conditions and the Ethical guidelines still apply. In no event shall the Royal Society of Chemistry be held responsible for any errors or omissions in this *Accepted Manuscript* or any consequences arising from the use of any information it contains.

ROYAL SOCIETY OF CHEMISTRY

www.rsc.org/faraday_d

CREATED USING THE RSC REPORT TEMPLATE (VER. 3.1) - SEE WWW.RSC.ORG/ELECTRONICFILES FOR DETAILS
REVIEW Faraday Discussions www.rsc.org/xxxxxx | XXXXXXXX

Comparison of Self-Assembled and Micelle Encapsulated QD Chemosensor Constructs for Biological Sensing

Christopher M. Lemon and Daniel G. Nocera*
DOI: 10.1039/b000000x

Whereas a variety of covalent conjugation strategies have been utilized to prepare quantum dot (QD)-based nanosensors, supramolecular approaches of self-assembly have been underexplored. A major advantage of self-assembly is the ability to circumvent laborious synthetic efforts attendant to covalent conjugation of a chemosensor to functionalized QDs. Here, we combine a CdSe/ZnS core-shell QD with gold(III) corroles using both self-assembly and micelle encapsulation to form QD nanosensors. Appreciable spectral overlap between QD emission and corrole absorption results in efficient Förster resonance energy transfer (FRET), which may be initiated by one- or two-photon excitation. The triplet state of the gold(III) corroles is quenched by molecular oxygen, enabling these constructs to function as optical O_2 sensors, which is useful for the metabolic profiling of tumours. The photophysical properties, including QD and corrole lifetimes, FRET efficiency, and O_2 sensitivity, have been determined for each construct. The relative merits of each conjugation strategy are assessed with regard to their implementation as sensors.

Introduction

The metabolic status of a tumour is well-characterized by the concentration of protons, glucose, and oxygen, as these parameters quantify tumour metabolism, consumption, and respiration, respectively.[1,2] Both pH and pO_2 are particularly relevant because the tumour microenvironment is characterized by low extracellular pH (6.6–6.8)[3] and hypoxia ($pO_2 \leq 5$ Torr).[2] Understanding how these parameters change as a function of disease progression or chemotherapy will enable clinicians to improve patient outcomes. To this end, new sensors are needed to monitor dynamic changes of biologically relevant analyte concentrations in real time. Additionally, these sensors must be small enough to penetrate into tumour tissue, enabling precise mapping of analyte gradients in tissue with high spatial resolution.

To meet these criteria, we have selected fluorescent semiconductor quantum dots (QDs) to serve as platform from which to assemble chemosensors for tumour imaging.[4] Fluorescent semiconductor QDs are ideal scaffolds for optical sensors because they are photostable and possess broad excitation profiles, narrow emission profiles, and high photoluminescence quantum yields.[5] The emission properties of suitably prepared QDs are unperturbed by environmental changes, such as the presence or absence of an analyte.[6] This enables ratiometric sensing, where the concentration of analyte is determined by measuring changes in emission intensity relative to an internal standard. Moreover, QDs have two-photon absorption cross

sections (σ_2) on the order of 10^4 Göppert–Mayer units (1 GM = 10^{-50} cm^4•s/photon),[7,8] which is substantially greater than typical organic fluorophores (σ_2 = 10–100 GM).[9,10] This property makes QD-based constructs superior chemosensors for multiphoton laser scanning microscopy (MPLSM), a technique that uses near-IR light (600–1100 nm) to exploit the tissue transparency window, where endogenous fluorophores do not absorb. Accordingly, MPLSM enables deep tissue penetration (450–600 μm) with approximately 1 μm spatial resolution.[11–13]

Since the photophysical properties of the QD are largely unaffected by analyte, the QD must be paired with an analyte-responsive fluorophore, furnishing a donor–acceptor pair.[14] The QD donor serves as the (multi)photon antenna and subsequently transfers this energy to the chemosensor active site. One of the most common methods of signal transduction in QD-based systems is Förster resonance energy transfer (FRET).[14] In this mechanism, energy is transferred from the donor to the acceptor through space via a long-range dipole–dipole interaction,[15] thereby decreasing the emission intensity of the QD donor. For a FRET sensor pair, the donor is selected for its absorption properties in a desired optical window, whereas the acceptor is selected for analyte sensitivity and desired optical properties that serve to measure analyte concentration. To maximize energy transfer in the dyad, the FRET pair must be judiciously selected such that the emission profile of the donor is energetically matched to the absorption profile of the acceptor. In this regard, QDs are ideal FRET donors because their emission profiles are tunable with size,[16] enabling facile matching of the emission spectrum to the absorption spectrum of the acceptor. Using these design principles,[4] we have developed a series of quantum dot based pH sensors,[17–19] as well as high- (160–760 Torr)[20] and low-pressure (0–160 Torr)[21,22] oxygen sensors.

We have exploited a variety of methods to prepare QD donor|acceptor dyads. The most common method is the covalent attachment of the acceptor to a functionalized ligand on the surface of a QD.[23–25] These polymers or dendrimers solubilize the QD in aqueous buffer and provide a functional handle, such as a terminal amine, to covalently attach an acceptor via amide bond formation. We have used this method to attach a variety of analyte-responsive dyes to water-soluble QDs: a squaraine dye (pH),[17] SNARF-5F (pH),[18] and Os(II) polypyridyl complexes (O_2).[20] As an alternative to covalent strategies, we have explored supramolecular self-assembly to exploit the surface chemistry of QDs. In this approach, the acceptor molecule has been modified with a functional group, such as a pyridyl ring, that binds directly on the QD surface. This is a rapid method of preparing conjugates and enables precise control of the donor–acceptor ratio. We have utilized this strategy for the preparation of self-assembled O_2 sensors comprised of *meso*-pyridyl Pd(II) porphyrins.[21] Since this method involves the displacement of hydrophobic surface ligands with hydrophobic fluorophores, self-assembled conjugates are restricted to organic solvents. In order to overcome this limitation, we have employed micelles as a means of transferring the organic-soluble constructs to an aqueous environment. Phospholipids modified with PEG chains were used to encapsulate preformed organic soluble assemblies using sonication processing. Their formation is templated by the QD, using hydrophobic interactions between the surface ligands and the oleate groups of the phospholipid. This method has been used to translate the Pd(II) porphyrin assemblies to an aqueous environment.[22]

Supramolecular approaches of QD donor|acceptor self-assembly bypass laborious synthetic efforts that are needed to covalently conjugate a chemosensor to QDs

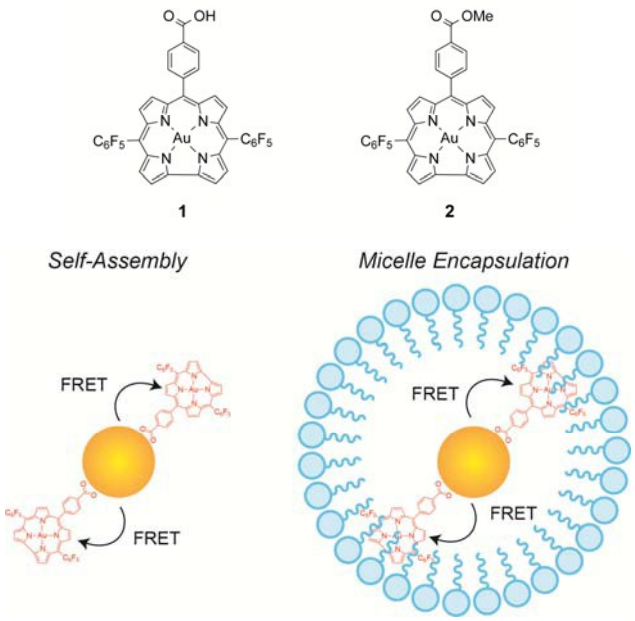

Figure 1. (Top) Chemical structures of the gold(III) corroles used for QD sensor construct. (Bottom) Schematic representations of the different strategies for conjugate formation explored in this study. A CdSe/ZnS core-shell quantum dot is paired with a Au(III) corrole as the O_2-sensitive phosphor. The corrole features a terminal carboxylic acid, which serves as a moiety for surfacing binding.

functionalized with multidentate polymers. Figure 1 depicts the QD donor|acceptor constructs that pair CdSe/ZnS core-shell QDs with gold(III) corroles **1** and **2**. With these constructs, the merits (analyte sensitivity, FRET efficiency, etc.) of self-assembled and micelle encapsulated constructs may quantitatively be compared. Gold(III) corroles were selected as the FRET acceptor for these conjugates because they have long-lived triplet states (~80 μs), rendering them O_2-sensitive phosphors in the biologically relevant 0–160 Torr O_2 range. Moreover, they emit in the near-IR (~790 nm), which is conducive to biological imaging and sensing in the tissue transparency window. Because these molecules are more red absorbing than isoelectronic palladium(II) and platinum(II) porphyrins, they may be paired with larger yellow-emitting (λ = 570 nm) QDs rather than green-emitting ones (λ = 525 nm). We have recently discussed the difficulties in using *in vivo* intensity data obtained from Pd(II) porphyrin-based sensors.[22] In this system, the green photons from the QD are scattered substantially more than the red photons from the porphyrin, thereby skewing the observed red:green ratio. The red shift of the corrole absorption features decreases the difference in donor and acceptor photon scatter as a function of depth. As a result, constructs with gold(III) corroles may enable *in vivo* intensity data to be used as a quantitative means of determining O_2 concentrations. As a result, dynamic changes may be monitored in real time without the need for measuring lifetimes across then entire field of view.

Compound **1** is well-suited for association to QD surfaces via the carboxylic acid moiety at the *meso* position of the corrole ring. The corresponding methyl ester (**2**) serves as a control, so that non-specific QD binding may be assessed. Compound **2**

also allows us to determine whether surface binding is a prerequisite for micelle incorporation. To the best of our knowledge, the constructs prepared in this study are the first examples of QD|corrole conjugates of any type.

Experimental Details

Preparation of Self-Assembled QD|Corrole Conjugates

Synthetic details for compounds **1** and **2** are provided in the Supporting Information. Toluene stock solutions of **1** and **2** (~400 μM) and **QD** (~40 μM) were prepared. An aliquot of the QD stock (typically containing ~0.8 nmol of QDs) was dissolved in 4 mL of toluene; an appropriate volume of the corrole stock was then added to give 10 molar equivalents of corrole per QD. The resultant mixture was stirred overnight at room temperature to allow equilibration of the corrole to the QD surface, furnishing conjugates **QD1** via a specific QD-corrole interaction and **QD2** via a non-specific QD-corrole interaction.

Preparation of Micelle-Encapsulated Constructs

To prepare the micelle constructs **QD1-MC** and **QD2-MC**, fresh samples of **QD1** and **QD2** were first prepared. After allowing the solutions to equilibrate overnight, solvent was removed by rotary evaporation and the residue was dissolved in 400 μL of the lipid solution. Solvent was removed and 4 mL of PBS was added. The mixture was then sonicated for 5 min using a VWR Symphony ultrasonic bath to give a red-orange, non-turbid solution. Aggregates were removed by filtering the solution through 0.45 μm and 0.20 μm syringe filters (Pall). The corrole-free construct **QD-MC** was prepared using the same micelle formation protocol outlined above.

Physical Measurements

All ^{1}H NMR spectra were recorded on a Varian Inova-500 NMR spectrometer at the Harvard University Department of Chemistry and Chemical Biology Laukien-Purcell Instrumentation Center and internally referenced to the residual solvent signal (δ = 7.26 for $CHCl_3$ in $CDCl_3$).[26] UV–vis absorption spectra were acquired using a Cary 5000 spectrometer (Agilent). Steady-state emission spectra were recorded on a Photon Technology International (PTI) QM4 fluorometer equipped with a 150 W Xe arc lamp and a Hamamatsu R2658 photomultiplier tube. Quantum yields of Au(III) corroles were calculated relative to 1,1′,3,3,3′,3′-hexamethylindotricarbocyanine iodide (HITCI) in EtOH (Φ_{ref} = 0.283),[27] while those of QDs were determined using Rhodamine 6G in EtOH (Φ_{ref} = 0.95)[28] as a reference. Samples for lifetime (τ_o) and quantum yield measurements, as well as and evacuated steady-state emission spectra were prepared using three cycles of freeze–pump–thaw (f-p-t) to pressures below 10^{-5} Torr. Solution oxygen measurements in toluene were made using an Ocean Optics NeoFox Phase measurement system equipped with a HIOXY-R probe for measurements in toluene, or a FOXY-HPT-1-PNA probe for measurements in PBS buffer. Calibration of the probe and determination of solution oxygen concentrations have been described elsewhere.[22] Bright field transmission electron micrographs (TEM) were recorded using a JEOL 2010 transmission electron microscope.

Nanosecond time-resolved emission measurements of corrole lifetimes were acquired using a previously reported system.[29,30] Pump light was provided by the third harmonic (355 nm) of a Quanta-Ray Nd:YAG laser (Spectra-Physics) operating

at 10 Hz. The pump light was passed through a BBO crystal in an optical parametric oscillator (OPO) yielding a visible frequency that was tuned to 570 nm. Excitation light was attenuated to 3–4 mJ per pulse for all experiments using neutral density filters. Emitted light was passed to an iHR320 monochromator (Horiba Scientific) and dispersed by a blazed grating (500 nm, 300 grooves/mm) centred at 785 nm. The entrance and exit slits of the monochromator were set to a spectral resolution of 4 nm. The signal was amplified by a photomultiplier tube (R928, Hamamatsu) and collected on a 1 GHz digital oscilloscope (9384CM, LeCroy); acquisition was triggered using a photodiode to collect scattered laser excitation light.

Femtosecond time-resolved emission measurements of QD lifetimes were acquired using a Libra-F-HE (Coherent) chirped-pulse amplified Ti:sapphire laser system, as previously described.[21] Excitation pulses of 480 nm were produced via sum–frequency generation of the signal; the pulse power was attenuated to 2–3 mW at the sample. Emission lifetimes were measured on a Hamamatsu C4334 Streak Scope streak camera, which has been described elsewhere.[31] The emission signal was collected over a 140 nm window centred at 575 nm using 100, 50, 20, 10, or 5 ns time windows; delays for these time windows were generated using a Hamamatsu C1097-04 delay unit. Two-photon emission spectra and lifetimes were generated using this Libra-F-HE (Coherent) laser system. Excitation pulses of 965 nm were generated using second harmonic generation of the idler; the pulse power was attenuated to 2–3 mW using neutral density filters and the beam was focused onto the sample using a 100 mm focal length lens. The emission spectrum was collected using a Hamamatsu C4334 Streak Scope streak camera in a 140 nm window centred at 570 nm.

Energy Transfer Analysis

The efficiency of energy transfer from the QD to the corrole was evaluated using Förster analysis:[15,32]

$$E = \frac{mk_{\mathrm{D-A}}}{mk_{\mathrm{D-A}} + \tau_{\mathrm{D}}^{-1}} = \frac{mR_0^6}{mR_0^6 + r^6} \quad (1)$$

where $k_{\mathrm{D-A}}$ is the rate of energy transfer, r is the average distance between the donor and acceptor, R_0 is the Förster distance, or the distance at which the energy transfer efficiency is 50%, and m is the number of acceptor molecules per donor. This quantity (E) can be measured experimentally:

$$E = 1 - \frac{\tau_{\mathrm{D-A}}}{\tau_{\mathrm{D}}} \quad (2)$$

where τ_D is the lifetime of the QD alone and $\tau_{\mathrm{D-A}}$ is the lifetime of the QD in the presence of corrole. R_0 is determined from the spectral overlap integral,

$$R_0^6 = \frac{9000(\ln 10)\kappa^2 \Phi_D}{128\pi^5 \mathrm{N} n^4} \int_0^\infty F_{\mathrm{D}}(\lambda)\, \varepsilon_{\mathrm{A}}(\lambda)\, \lambda^4 \mathrm{d}\lambda \quad (3)$$

where κ^2 is the relative orientation factor of the dipoles, taken to be 0.476 for static donor-acceptor orientations,[32,33] Φ_{D} is the quantum efficiency of the donor, N is Avogadro's number, n is the index of refraction of the medium, which is taken to be 1.334 for PBS[34] and 1.4961 for toluene,[35] $F_{\mathrm{D}}(\lambda)$ is the normalized intensity of the

donor, and $\varepsilon_A(\lambda)$ is the extinction coefficient of the acceptor at wavelength λ. The latter half of this equation is known as the spectral overlap integral and is denoted by the variable *J*. The average number of corroles attached to the QD (*m*) was determined from the optical cross-sections of the spectra of QD, the corrole, and the corresponding assembly. The value for *m* and the concentration of the assemblies was calculated using the individual donor and acceptor absorption spectra, their known ε values, and Beer's law.

Results

Corrole Binding Studies

Titration experiments were performed to assess the surface binding of gold corroles **1** and **2** to the surface of **QD** in toluene via the following equilibrium:

$$\mathrm{QD} + \mathrm{Cor} \underset{K_D}{\overset{K_A}{\rightleftharpoons}} \mathrm{QD|Cor} \qquad (4)$$

with an equilibrium binding constant K_A. With increasing concentrations of corrole, the equilibrium is driven to conjugate formation; this process is conveniently monitored using the QD emission. For these studies, the QD was selected so that its emission profile overlaps with the Q(0,0) absorbance feature at 568 nm for corroles **1** and **2**. The absorption and emission spectra for **1** and **2** are provided in Figure S1. In order to maximize spectral overlap with the corrole acceptors, the QD used in this study has a first absorption feature at 562 nm and an emission band (λ_{exc} = 470 nm) centred at 572 nm (Figure S2). These QDs are natively capped with a mixture of oleic acid and oleylamine. In order to further characterize these QDs, bright field TEM images were acquired (Figure S3) and show that these QDs have a diameter of 5.76 ± 0.62 nm (61 independent QD measurements over 14 different images). The relatively large size of these particles suggests that each QD may easily accommodate several corrole acceptors.

The quenching of QD luminescence via energy transfer was examined for corrole **1** bearing a single carboxylic acid and the corresponding methyl ester **2**. The latter serves as a control to assess non-specific binding interactions with the QD. Titrations were performed in which the same amount of QD (~0.8 nmol or ~200 nM) was treated with 1, 2, 5, or 10 equivalents of **1** or **2**. Each sample point in the titration was prepared independently and incubated overnight to ensure corrole binding. Figure 2 shows the absorption, steady-state emission, and time-resolved emission profiles for the titration of QD with **1**. Similar data for compound **2** is presented in Figure S4.

The absorption profile (Figure 2a) is dominated by corrole absorption. Both steady state (Figure 2b) and time-resolved (Figure 2c) QD emission data shows that the photoluminescence is quenched upon the addition of **1**. Using both types of quenching data, the equilibrium constant (K_A) for conjugate formation (Eq. 4) was determined. This value may be calculated using the Stern–Volmer equation:

$$\frac{I_0}{I} = \frac{\tau_0}{\tau} = 1 + K_A[\mathrm{Cor}] \qquad (5)$$

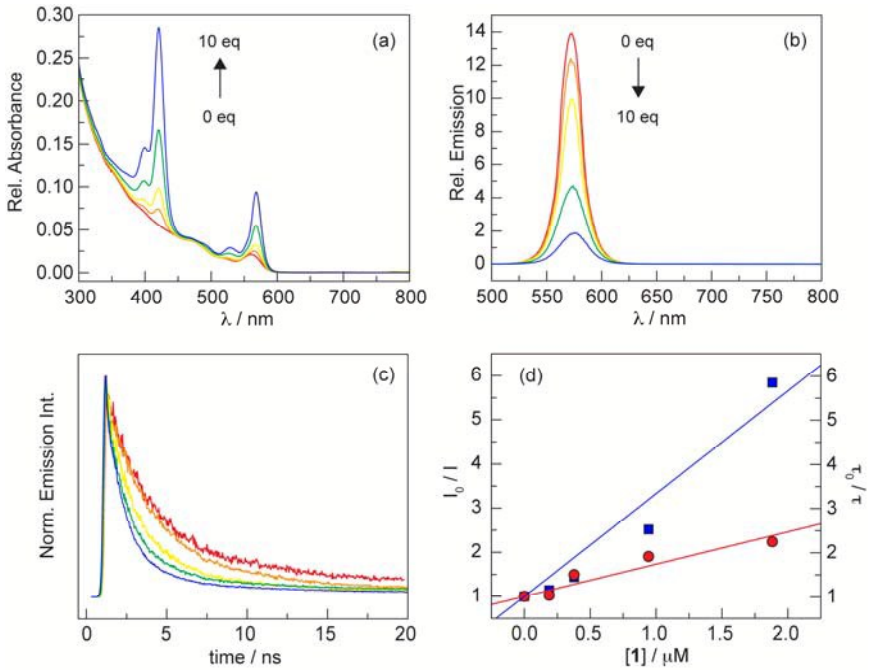

Figure 2. Spectral changes associated with the titration of a toluene solution of **QD** (—) with 1 (—), 2 (—), 5 (—), and 10 (—) equivalents of **1**. (a) The intensity of the Soret and Q bands of the corrole increase. (b) The QD emission (λ_{ex} = 470 nm) intensity, as well as the photoluminescence decay traces (c) of QD lifetime (λ_{ex} = 480 nm) decrease with increasing concentration of **1**. (d) Stern-Volmer plot to determine the equilibrium binding constant using both intensity data (■) from (b) and lifetime data (●) from (c) to give K_A values of 2.33×10^6 M^{-1} and 0.73×10^6 M^{-1}, respectively.

where I_0 and τ_0 are the emission intensity and lifetime, respectively, in the absence of added corrole, and I and τ are the emission intensity and lifetime, respectively, in the presence of a given corrole concentration [Cor]. The binding constants for compounds **1** and **2** are summarized in Table S1. Both emission and lifetime quenching titration data were fit to Eq. 5 to give the following average values of K_A = 1.62×10^6 M^{-1} (**1**) and 4.86×10^4 M^{-1} (**2**). As expected, corrole **1** with a carboxylic is able to strongly bind to the QD surface and efficiently quench QD luminescence. Conversely, the methyl ester derivative (**2**) interacts non-specifically with the QD and has an effective binding constant that is ~10^2 times weaker. It should be noted that no binding saturation is observed for either compound over this concentration range. Indeed, a linear quenching response is observed up to 20 equivalents of **1** (Figure S5). This implies that all 10 equivalents of the added corrole are in some way associated with the QD, either surface bound in the case of **1** or intercalated in the exterior capping ligands for **2**.

Characterization of Self-Assembled Constructs

Given the results of the titration studies, corroles **1** and **2** associate with the QD with a high enough binding constant to drive the equilibrium of Eq. 4 to conjugate formation. The self-assembled constructs with corroles **1** and **2**, **QD1** and **QD2**, respectively, were prepared using 10 equivalents of donor. The absorption spectrum of the conjugates is a composite of QD and corrole absorption features; the corrole

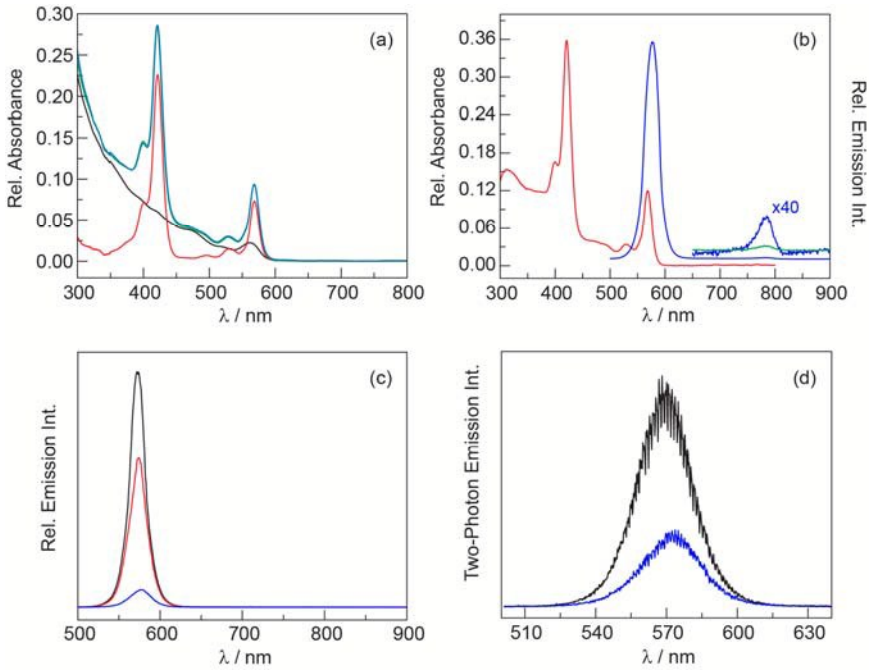

Figure 3. (a) Comparison of the absorption spectra of **1** (—), **QD** (—), and **QD1** (—) in toluene, showing that the conjugate is effectively the sum (—) of the two components. (b) Absorption (—) and emission (—) spectra (λ_{exc} = 470 nm) of a freeze–pump–thawed sample of **QD1** in toluene. For clarity, the corrole emission intensity was increased by a factor of 40. To illustrate the FRET enhancement in the conjugate, a concentration-matched sample of **1** (—) is also shown. (c) Emission spectra (λ_{exc} = 470 nm) of **QD** (—), **QD1** (—), and **QD2** (—) in toluene at equivalent quantum dot loading. (d) Two-photon emission spectra (λ_{exc} = 965 nm) of **QD** (—) and **QD1** (—) in toluene at equivalent quantum dot loading.

Soret and Q bands are superimposed onto the broad absorption profile of **QD** (Figure 3a). The emission spectrum (λ_{exc} = 470 nm) of the conjugates is dominated by emission from the QD (Figure 3b). In the conjugates, the emission maximum is red shifted 2–6 nm (60–180 cm^{-1}) relative to **QD** (Table 1). While the emission from the acceptor is weak, it is present; the low intensity is due to the low phosphorescence quantum yield of Au(III) corroles (0.2–0.3%). In the 500–900 nm region, the acceptor emission is clearly visible only for **QD1**, as the QD emission is substantially quenched. For **QD2**, QD emission is so strong that phosphorescence from **2** is within the baseline of the spectrum. However, if the scan is limited to the corrole region (650–900 nm), acceptor emission is visible in all cases.

In accordance with titration studies, the QD lifetime is greatly affected by the presence of corrole acceptor. The QD lifetime data for all constructs is summarized in Table 1. The lifetimes observed for **QD1** are much shorter than that of **QD2**, which reflects the binding efficiency observed in the titration studies due to static quenching of QD photoluminescence. In the absence of acceptor, the QD exhibits monoexponential decay kinetics (R_{adj}^2 > 0.99) with a lifetime of about 5 ns. Typically, bi- or tri-exponential kinetics are observed to account for multiple phenomena, such as surface trapped states, exciton emission, and Auger recombination.[36,37] In this case, the observance of monoexponenital kinetics is likely

Table 1. Summary of QD Photoluminescence Data

Construct	λ_{em} [a]	τ_1 (ns)	A_1 (%) [b]	τ_2 (ns)	A_2 (%) [b]	ϕ_f [c]	E [d]
QD	572	4.93 ± 0.20	100%	–	–	0.70	–
QD$_{2hv}$	568	15.09 ± 0.23	34%	1.48 ± 0.05	66%	–	–
QD1	578	2.24 ± 0.07	15%	0.55 ± 0.01	85%	0.05	0.84
QD1$_{2hv}$	572	1.36 ± 0.08	15%	0.29 ± 0.01	85%	–	0.93
QD2	574	7.22 ± 0.52	19%	3.06 ± 0.28	81%	0.44	0.22
QD-MC	575	14.81 ± 3.61	37%	5.96 ± 0.45	63%	0.14	–
QD1-MC	577	2.17 ± 0.16	12%	0.43 ± 0.04	88%	0.01	0.93
QD2-MC	577	7.99 ± 0.86	16%	2.19 ± 0.37	84%	0.02	0.66

[a] Observed transitions with λ_{exc} = 470 nm (or 965 nm for 2hv excitation), [b] Relative contribution to the biexponential fit, [c] Fluorescence quantum yield, relative to Rhodamine 6G in EtOH (ϕ_f = 0.95), [d] FRET efficiency calculated using Eq. 2, Errors associated with each measurement are reflective of 1 standard deviation

due to efficient passivation of surface trapped states due to the presence of a sufficiently thick ZnS shell. Conversely, the conjugates **QD1** and **QD2** exhibit biexponential kinetics ($R_{adj}^2 > 0.99$). This is likely a result of the perturbation of the QD surface as a result of corrole binding, which induces surface-trapped states that were not present in the absence of acceptor. Indeed, the long component of the fit (~7 ns, 20%) is consistent with surface-trapped states, whereas the short component (~3 ns, 80%) is comparable to the exciton emission lifetime observed for **QD** (~5 ns).

QD photoluminescence quenching is a direct result of Förster resonance energy transfer (FRET) as a result of significant spectral overlap between QD emission and acceptor absorption (Figure S6). This interaction has been characterized using both steady-state and time-resolved methods. For **QD1** and **QD2**, the photoluminescence intensity is decreased by 93% and 38%, respectively, compared to native QD (Figure 3c). This data is consistent with the observed decreases in photoluminescence quantum yield (Table 1). **QD2** exhibits only a 37% decrease in quantum yield relative to QD, whereas a 93% decrease is observed for **QD1**. Using the lifetime data of Table 1 and Eq. 2, the FRET efficiency in each conjugate is determined to be 84% for **QD1** and 22% for **QD2**. A summary of FRET parameters is presented in Table S2. For both constructs, the spectral overlap integral (J) and Forster distance (R_0) are quite similar. However, the less efficient binder **QD2** has an average donor–acceptor distance (r) that is ~3.4 nm longer than for **QD1** (r = 5.70 nm).

FRET is supported by excitation spectra (Figure S7) recorded by monitoring the corrole emission at 780 nm. The collected emission is attributed to corrole, as QD emission is spectrally separated by over 200 nm. At wavelengths where **1** and **2** do not readily absorb (λ < 370 nm), a substantial emission signal is observed. QD absorbance dominates in this spectral region, demonstrating that it is the donor in the FRET process. Additional evidence for FRET is revealed upon comparison of the corrole emission in the conjugate relative to the free acceptor. Under linear excitation at 470 nm where the QD is the primary absorber, there is a six-fold enhancement in T(0,0) emission intensity for **QD1** relative to a concentration-matched solution of **1** (Figure 3b). In the conjugate, the QD serves as a photon antenna and the absorbed energy is transferred to the appended corrole, resulting in a FRET-based enhancement in acceptor emission.

Table 2. Summary of Au Corrole Phosphorescence Data

Construct	τ_{air} (μs)	τ_0 (μs)[a]	k_q[b]	ϕ_p[c] × 10^2	k_r[d] (s^{-1})	k_{nr}[d] (s^{-1})
1	0.63 ± 0.01	84.2 ± 0.5	8.6×10^8	0.24	28	1.18×10^4
2	0.62 ± 0.01	82.0 ± 1.7	8.3×10^8	0.32	39	1.22×10^4
QD1	0.88 ± 0.04	100.3 ± 0.9	6.5×10^8	0.43	42	0.99×10^4
QD2	0.78 ± 0.05	93.7 ± 2.6	1.0×10^9	0.50	54	1.06×10^4
QD1-MC$_{long}$[e]	2.32 ± 0.04 (75)[f]	81.9 ± 2.7 (85)	1.6×10^9	0.33	40	1.22×10^4
QD1-MC$_{short}$	0.52 ± 0.05 (25)	21.1 ± 4.1 (15)	8.4×10^9	0.33	155	4.72×10^4
QD2-MC$_{long}$	2.02 ± 0.19 (57)	103.8 ± 4.3 (85)	2.1×10^9	0.37	36	0.96×10^4
QD2-MC$_{short}$	0.59 ± 0.11 (43)	30.7 ± 5.4 (15)	9.3×10^9	0.37	120	3.25×10^4

[a] Freeze–pump–thawed samples (f-p-t) (< 10^{-5} Torr) with λ_{ex} = 570 nm, [b] Calculated using Eq. 7, [c] Phosphorescence quantum yield, relative to HITCI in EtOH (ϕ = 0.283) for f-p-t samples, [d] Calculated using Eq. 6, [e] Biexponential kinetics were observed for the micelle constructs; long and short refer to the two components, [f] Relative contribution to the biexponential fit, Errors associated with each measurement are reflective of a 95% confidence interval

In addition to characterization of the system under linear excitation, the conjugates were studied under two-photon excitation (λ_{exc} = 965 nm). The integrated emission intensity from the QD in **QD1** is reduced by 63% relative to **QD** alone (Figure 3d). Additionally, QD lifetime measurements were made under two-photon excitation conditions (Table 1). In this case, **QD** exhibits the expected biexponential decay kinetics ($R_{adj}^2 > 0.99$), with a long component of 15 ns due to surface trapped states and a short component of 1.5 ns due to exciton emission. The observed difference in lifetime under one- and two-photon excitation is a result of a difference in selection rules.[38,39] The QD lifetime for **QD1** is substantially quenched. Using the amplitude-weighted average lifetimes, a FRET efficiency of 93% is calculated, assuming that the quantum yield of the QD is the same under both linear and two-photon excitation. This corresponds to an average donor–acceptor distance (r) of 4.88 nm (Table S2), which is approximately 1 nm shorter than the value calculated under linear excitation.

Triplet lifetimes of the free corroles and conjugates **QD1** and **QD2** were recorded in toluene for aerated and f-p-t and the data is presented in Table 2. Decay traces at t > 100 ns were fit to a monoexponential decay function ($R_{adj}^2 > 0.99$). Corroles **1** and **2** exhibit natural radiative lifetimes of 82–84 μs. The phosphorescence quantum yields for this transition was measured to be 0.24% and 0.32% for compounds **1** and **2**, respectively. Upon conjugate formation, the lifetime is increased by 16 μs for **QD1** and 12 μs for **QD2**. This increase in lifetime is accompanied by a ~1.7 fold increase in the phosphorescence quantum yield to 0.43% for **QD1** and 0.50% for **QD2**. The quantum yield and lifetime are correlated according to the following equation:

$$\phi = \frac{k_r}{k_r + k_{nr}} = k_r \tau_0 \qquad (6)$$

where ϕ is the phosphorescence quantum yield, τ_0 is the phosphorescence lifetime, k_r is the radiative rate constant, and k_{nr} is the nonradiative rate constant. Using the data of Table 2, these rate constants may be estimated for both the compounds and their conjugates. Upon conjugate formation, k_{nr} decreases by ~15% while k_r increases by 40–50%.

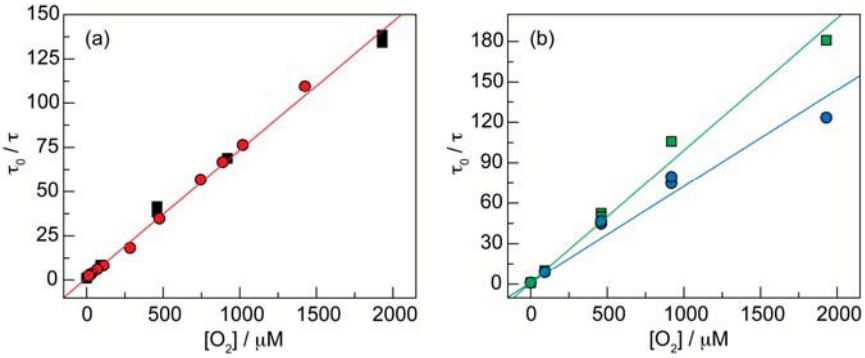

Figure 4. (a) Stern–Volmer plot for compound **1** in toluene, constructed from data using pre-mixed gases (■) and variable O_2 concentrations (●), as measured using a fiber optic probe. (b) Stern–Volmer plot for **QD1** (●) and **QD2** (■) in toluene using pre-mixed gases.

Quenching of the triplet state by molecular oxygen was quantified using the Stern–Volmer relation:

$$\frac{\tau_0}{\tau} = 1 + k_q \tau_0 [O_2] \qquad (7)$$

where τ_0 is the natural radiative lifetime of the phosphor in the absence of quencher, τ is the lifetime of the phosphor at a given oxygen concentration $[O_2]$, and k_q is the bimolecular quenching rate constant. Each construct was studied in toluene, purging the sample with five different gases to construct a Stern-Volmer plot: ambient air (1930 μM O_2), 10 % O_2 (919 μM O_2), 5 % O_2 (460 μM O_2), 1 % O_2 (92 μM O_2), and argon (0 μM O_2). Variable O_2 measurements were made using a HIOXY fibre optic oxygen sensor after purging the sample with argon for corroles **1** and **2**. The Stern-Volmer data is presented for compound **1** in Figure 4a and constructs **QD1** and **QD2** in Figure 4b. The bimolecular quenching constant for **1** was found to be 8.6×10^8 M^{-1} s^{-1}, and that of **2** is 8.3×10^8 M^{-1} s^{-1}). Upon conjugate formation, k_q decreases by ~25% for **QD1**, whereas k_q increases by ~25% for **QD2**, relative to the free phosphor. Thus, the oxygen sensitivity of the corrole is minimally perturbed in the conjugate.

Characterization of Micelle Constructs

In order to prepare the water-soluble micelle constructs, preformed conjugates **QD1** and **QD2** were encapsulated in a phosphoethanolamine lipid modified with a PEG-2000 chain[40] using sonication processing[22] to afford micelles **QD1-MC** and **QD2-MC**, respectively. For comparison, corrole-free micelles **QD-MC** were prepared in analogous way without the addition of an acceptor (Figure S8). The steady-state absorption and emission spectra of these constructs are quite similar to the toluene-soluble analogues. Examination of the absorbance spectra reveals that 10 and 9 equivalents of acceptor are incorporated into **QD1-MC** and **QD2-MC**, respectively (Figure S9). With regard to the emission spectra (λ_{exc} = 470 nm), corrole emission is barely perceptible above the baseline when scanning over the 500–900 nm region for **QD1-MC** and **QD2-MC**. When examining the corrole region (650–900 nm) separately, acceptor emission is visible.

For these CdSe/ZnS QDs, micelle encapsulation drastically diminishes the

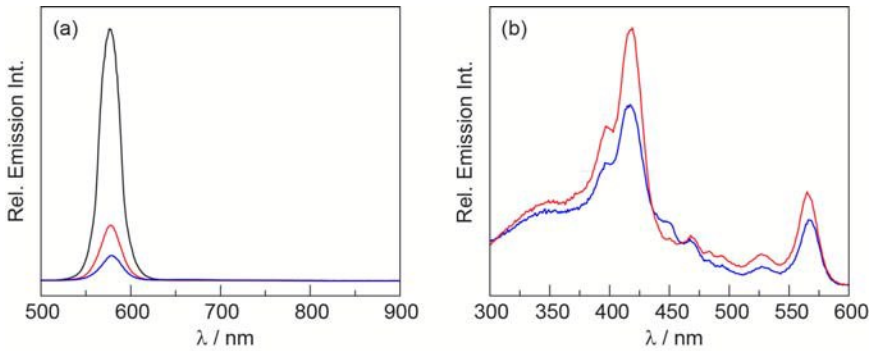

Figure 5. (a) Emission spectra (λ_{ex} = 470 nm) of **QD-MC** (—), **QD1-MC** (—), and **QD2-MC** (—) in PBS at equivalent quantum dot loading. (b) Excitation spectra (λ_{exc} = 780 nm) of concentration matched solutions of **QD1-MC** (—) and **QD2-MC** (—) in PBS.

photoluminescence quantum yield, from 70% for **QD** in toluene to only 14% for **QD-MC** in PBS. This perturbation of the QD surface also manifests in the photoluminescence decay kinetics (Table 1). Whereas a monoexponential decay was observed for **QD**, **QD-MC** displays biexponential kinetics with a long ~15 ns component reflective of surface trapped states and a short ~6 ns component due to exciton emission. The relative amplitudes of these components is nearly identical to that observed for **QD** under two-photon excitation. Upon incorporation of corrole acceptors, the lifetime decreases; the relative amplitudes of both components are similar to those observed for **QD1** and **QD2**. As expected, the decrease in photoluminescence lifetime is more substantial for **QD1-MC** than **QD2-MC**, akin to the results observed for the organic soluble constructs.

The FRET interaction between the QD donor and corrole acceptors in the micelle constructs was characterized using both steady-state and time-resolved methods. Due to a 3 nm (90 cm^{-1}) red shift in the emission spectrum **QD-MC** relative to QD, the spectral overlap in the micelle constructs is nominally decreased (Figure S10). For **QD1-MC** and **QD2-MC**, the photoluminescence intensity is decreased by 90% and 78%, respectively, compared to **QD-MC** (Figure 5a). Using the lifetime data of Table 1 and Eq. 2, the FRET efficiency for **QD1-MC** is 93% while this value is 66% for **QD2-MC**, which is a substantial increase relative to **QD2** in toluene (22%). A summary of the FRET parameters is presented in Table S2. The Förster distance (R_0) for the micelles is ~1 nm shorter than for the self-assembled constructs. The primary reason for this is the substantial decrease in the photoluminescence quantum yield of the donor (see Eq. 3). This manifests in a substantial decrease in the average donor–acceptor distance r for both micelle constructs. However, the distance r for **QD2-MC** is ~1.3 nm longer than that for **QD1-MC** (r = 3.94 nm). The FRET interaction is also observed in the excitation spectra of the micelles (Figure 5b). As observed for the organic soluble assembles, substantial emission signal is observed at $\lambda < 370$ nm where QD absorption dominates, indicating that it is the FRET donor.

Triplet corrole lifetimes were measured for both aerated and f-p-t samples of **QD1-MC** and **QD2-MC** in PBS. Decay traces at $t > 100$ ns were fit to a biexponential decay function ($R_{adj}^2 > 0.99$) and the results are summarized in Table 2. For f-p-t samples, the long component (85% relative amplitude) of **QD1-MC** is similar to the lifetime of **1** alone; in the case of **QD2-MC**, it is longer than that

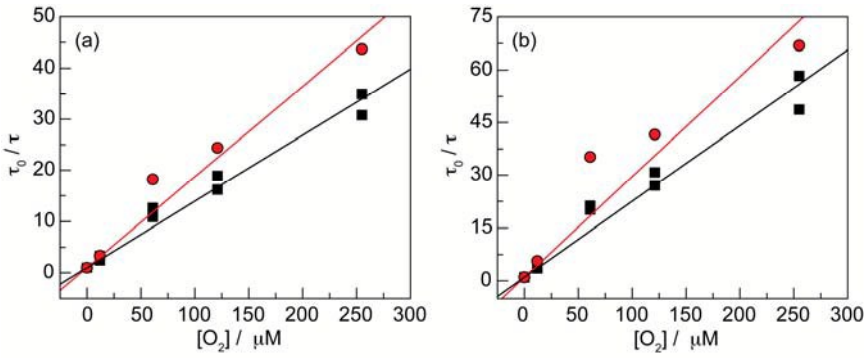

Figure 6. Stern–Volmer plots for (a) **QD1-MC** and (b) **QD2-MC** in PBS. These plots were constructed using pre-mixed gases. Each plot shows the long (■) and short (●) components of the biexponential fit.

observed for either **2** or **QD2**. In both cases, the short component (15% relative amplitude) is substantially shorter (20–30 μs). The phosphorescence quantum yields are higher than the free acceptor (1.4 fold increase for **QD1-MC**), but they are not as high as those observed for the toluene soluble analogues. Using the lifetimes and quantum yields, we may estimate k_{nr} and k_r using Eq. 6. Since the lifetimes are biexponential and the quantum yield is a steady-state measurement that cannot disentangle the two components, the values for the rate constants can only be bracketed. For both micelle constructs, the values of both the radiative and non-radiative rate constants are similar: k_r = 35–155 s^{-1} and k_{nr} = 1–5 × 10^4 s^{-1}.

The oxygen sensitivity of **QD1-MC** and **QD2-MC** is maintained in PBS. Each sample was purged with five different gases to construct a Stern–Volmer plot: ambient air (255 μM O_2), 10 % O_2 (121 μM O_2), 5 % O_2 (61 μM O_2), 1 % O_2 (12 μM O_2), and argon (0 μM O_2). All data fit to a biexponential decay function and each component was analysed according to Eq. 7. The data from these experiments is plotted in Figure 6 for both the long and short component of each construct. The long component is well-behaved and exhibits a bimolecular quenching rate constant that is 1.9–2.5 times longer than the k_q determined for the free corroles (2 × 10^9 M^{-1} s^{-1}). The short component is substantially more variable, but reasonable fits (R_{adj}^2 > 0.938) were obtained. It was found that this data gave values of k_q that are near the diffusion limit (8–9 × 10^9 M^{-1} s^{-1}).

Discussion

Supramolecular assembly of QD-based donor–acceptor FRET pairs represents a rapid and facile method of conjugate formation. It enables precise control over the donor–acceptor ratio and circumvents the laborious synthesis of multidentate amphiphilic polymers. Consistent with the observation that fluorophores with terminal carboxylic acids efficiently bind to the surface of QDs,[41,42] the equilibrium constant for the association **1** to QD is 1.62 × 10^6 M^{-1}. The binding of the carboxylic acid moiety of **1** proceeds by ligand exchange at surface Zn(II) ions, displacing the native oleic acid ligand. This value is quite similar to the K_A for the surface binding of a Pd(II) porphyrin with a single 4-pyridyl substituent: 1.36 × 10^6 M^{-1}.[21] For porphyrins, we[21] and others[43,44] have shown that two adjacent binding

groups in a *cis* disposition have binding constants that are an order of magnitude higher. As a result, a *cis*-A_2B derivative of **1** or an A_3 tri-carboxylic acid corrole, though synthetically more challenging,[45] will likely further increase the association constant and lead to higher FRET efficiencies, and by extension, the emission signal from the acceptor. Based the lower $K_A = 4.86 \times 10^4$ $M^{-1}$for **2**, non-specific binding of corrole to QD is not significant. Quenching of QD emission by **2** only occurs at high equivalency of the acceptor. The substantially longer FRET distance *r* between the QD and **2** (9.12 nm) as compared to **1** (5.70 nm) suggests that the non-specific interaction is derived from the intercalation of compound within the hydrophobic capping ligands of the QD.

The phosphorescence lifetime **QD1** and **QD2** in toluene exhibits monoexponential decay kinetics, indicating a homogeneous environment (surface bound to the QD in **1** and dispersed in the capping ligands for **2**). The lifetimes of the corroles in conjugates **QD1** and **QD2** are longer than the free phosphor, thus leading to an increase in the phosphorescence quantum yield. The greater increase for **QD1** as compared to **QD2** indicates that surface binding constrains the geometry of the corrole and results in attenuated nonradiative decay processes relative to non-specifically associated corrole with the surface ligands.

Encapsulation of the pre-formed organic soluble conjugates **QD1** and **QD2** proceeds facilely by sonication. All of the corrole equivalents in **QD1** are associated to the QD surface, and hence they are carried into the micelle **QD1-MC**. We note however, that high loadings are also achieved **QD2-MC**; the absorption spectrum of construct indicates that 9 out of the 10 added equivalents of **2** were incorporated into the micelle, demonstrating that surface binding is not a pre-requisite for incorporation of the acceptor into the micelle: non-specific interactions with the QD surface ligand are sufficient. Notwithstanding, surface binding of the acceptor leads to a high FRET efficiency: $E = 0.93$ for **QD1-MC** vs. $E = 0.66$ for **QD2-MC**. With the increase in FRET efficiency of **QD1-MC** relative to **QD1**, in conjunction with the decrease in quantum yield of **QD-MC** relative to the native QD, the average donor–acceptor distance decreases from 5.70 nm in **QD1** to 3.94 nm in the micelle. This distance corresponds to the measured metrics of each component. Based on the bright field TEM data of Figure S3, the radius of the QD is 2.88 nm. From the crystal structure of compound **2**, the distance between the methyl group of the ester (in order to approximate the bond between the carboxylate group and the metal atom on the QD surface) and the gold centre is 1.11 nm. The QD to corrole centre-to-centre distance based on structural metrics is 3.99 nm, which is remarkably similar to the calculated value of 3.94 obtained from FRET measurements.

The phosphorescence lifetime of the corrole in both constructs, **QD1-MC** and **QD2-MC**, exhibits biexponential decay kinetics, indicating that the corrole resides in two distinct environments within the micelle. The long component is attributed to corrole associated with the QD surface, while the short component is ascribed to free corrole residing within the micelle. These results are consistent with our observations for the QD|porphyrin micelles, where biexponential kinetics were observed for the Pd(II) porphyrin.[22] For the corrole conjugates, each component exhibits a linear Stern–Volmer relationship as a function of oxygen. The long component is well behaved and exhibits a bimolecular quenching constant (k_q) that is $\sim 2 \times 10^9$ M^{-1} s^{-1}; the short component of $\sim 9 \times 10^9$ M^{-1} s^{-1} is at the diffusion limit. For sensing applications only corroles at the surface of the QD can be excited via FRET by two photon excitation because the QD is the two photon antenna. Free

corrole within the micelle cannot be excited, and hence emission decay from this population is absent under two-photon excitation conditions. In this regard, the two-photon experiment is ideal for *in vivo* sensing for self-assembled chemosensors, as the experiment naturally selects for a single population of chemosensors which are associated to the QD. Background signal from unassociated chemosensors is absent, since this population cannot directly be excited under two photon conditions. This is a powerful property of the micelle approach for sensing applications.

Conclusions

Micelle encapsulation represents a scalable method of synthesizing QD nanosensors and circumvents laborious multi-step polymer syntheses required for coating QDs for covalent conjugation to a chemosensor. Using this technique, here we demonstrate self-assembled and micelle encapsulated conjugates of Au(III) corroles and CdSe/ZnS QDs. For the organic soluble assemblies, all of the corrole equivalents associate with the QD in some way: surface bound in the case of the carboxylic acid **1**, or loosely associated with the capping ligand at the solvent interface for the methyl ester **2**. Because of the efficient surface binding of **1**, static quenching of QD photoluminescence and FRET efficiency are much greater than for **2**. Due to the large size of the QD, all of the added corrole equivalents are associated with the QD as supported by the observation of monoexponential decay kinetics of corrole phosphorescence and the incorporation of all the added corrole equivalents into the micelle. Within the micelle, the corrole phosphorescence exhibits biexponential decay owing to acceptor residing in two distinct environments within the micelle: corrole tightly bound or associated with the QD surface (long component) and free corrole dispersed in the lipids of the micelle (short component). In terms of O_2 sensing, the long component is well behaved and may serve as a robust metric for sensing oxygen as this is the only population that may be excited under two-photon conditions. These results establish micelle encapsulation as an ideal vehicle to implement sensing via FRET signal transduction pathways of QD-donor|acceptor constructs.

Acknowledgements

This material is based upon work supported by the U.S. Department of Energy Office of Science, Office of Basic Energy Sciences under Award No. DE-SC0009758. C.M.L. acknowledges the National Science Foundation's Graduate Research Fellowship Program. We thank Yue Chen for preparing the CdSe/ZnS quantum dots, Andrew Maher for assistance with experiments using the Libra-F-He laser system, and Dr. Thomas Kempa for acquiring the TEM images.

References

Department of Chemistry and Chemical Biology, Harvard University, 12 Oxford Street, Cambridge, Massachusetts 02138, United States. Fax: +1 617-496-0265; Tel: +1 617-495-8904; E-mail: dnocera@fas.harvard.edu

† Electronic Supplementary Information (ESI) available: Synthetic methods for the preparation of compounds **1** and **2**, as well as NMR spectra, TEM images of CdSe/ZnS quantum dots, additional spectroscopic characterization of the conjugates, and tables of spectrsocopic data including binding constants and FRET parameters. See DOI: 10.1039/b000000x/

1 P. Vaupel, F. Kallinowski and P. Okunieff, *Cancer Res.*, 1989, **49**, 6449–6465.
2 G. Helmlinger, F. Yuan, M. Dellian and R. K. Jain, *Nat. Med.*, 1997, **3**, 177–182.
3 G. Helmlinger, A. Sckell, M. Dellian, N. S. Forbes and R. K. Jain, *Clin. Cancer Res.*, 2002, **8**, 1284–1291.
4 C. M. Lemon, P. N. Curtin, R. C. Somers, A. B. Greytak, R. M. Lanning, R. K. Jain, M. G. Bawendi and D. G. Nocera, *Inorg. Chem.*, 2014, **53**, 1900–1915.
5 C. B. Murray, D. J. Norris and M. G. Bawendi, *J. Am. Chem. Soc.*, 1993, **115**, 8706–8715.
6 G. W. Walker, V. C. Sundar, C. M. Rudzinski, A. W. Wun, M. G. Bawendi and D. G. Nocera, *Appl. Phys. Lett.*, 2003, **83**, 3555–3557.
7 S. A. Blanton, A. Dehestani, P. C. Lin and P. Guyot-Sionnest, *Chem. Phys. Lett.*, 1994, **229**, 317–322.
8 D. R. Larson, W. R. Zipfel, R. M. Williams, S. W. Clark, M. P. Bruchez, F. W. Wise and W. W. Webb, *Science*, 2003, **300**, 1434–1436.
9 C. Xu and W. R. Zipfel, Multiphoton Excitation of Fluorescent Probes, *Handbook of Biomedical Nonlinear Optical Microscopy*, B. R. Master and P. T. C. So, Eds., Oxford University Press, 2008, pp 311–333.
10 C. Xu and W. W. Webb, *J. Opt. Soc. Am. B*, 1996, **13**, 481–491.
11 C. Xu, W. Zipfel, J. B. Shear, R. M. Williams and W. W. Webb, *Proc. Natl Acad. Sci. U.S.A.*, 1996, **93**, 10763–10768.
12 W. R. Zipfel, R. M. Williams and W. W. Webb, *Nat. Biotechnol.*, 2003, **21**, 1369–1377.
13 R. K. Jain, M. F. Booth, T. P. Padera, L. L. Munn, D. Fukumura and E. Brown, Applications of Nonlinear Intravital Microscopy in Tumor Biology, *Handbook of Biomedical Nonlinear Optical Microscopy*, B. R. Master and P. T. C. So, Eds., Oxford University Press, 2008, pp 735–756.
14 R. C. Somers, M. G. Bawendi and D. G. Nocera, *Chem. Soc. Rev.*, 2007, **36**, 579–591.
15 T. Förster, *Ann. Phys.*, 1948, **437**, 55–75.
16 A. P. Alvisatos, *J. Phys. Chem.*, 1996, **100**, 13226–13239.
17 P. T. Snee, R. C. Somers, G. Nair, J. P. Zimmer, M. G. Bawendi and D. G. Nocera, *J. Am. Chem. Soc.*, 2006, **128**, 13320–13321.
18 R. C. Somers, R. M. Lanning, P. T. Snee, A. B. Greytak, R. K. Jain, M. G. Bawendi and D. G. Nocera, *Chem. Sci.*, 2012, **3**, 2980–2985.
19 E. R. Kay, J. Lee, D. G. Nocera and M. G. Bawendi, *Angew. Chem., Int. Ed.*, 2013, **52**, 1165–1169.
20 E. J. McLaurin, A. B. Greytak, M. G. Bawendi and D. G. Nocera, *J. Am. Chem. Soc.*, 2009, **131**, 12994–13001.
21 C. M. Lemon, E. Karnas, M. G. Bawendi and D. G. Nocera, *Inorg. Chem.*, 2013, **52**, 10394–10406.
22 C. M. Lemon, E. Karnas, X. Han, O. T. Bruns, T. J. Kempa, D. Fukumura, M. G. Bawendi, R. K. Jain, D. G. Duda and D. G. Nocera, *J. Am. Chem. Soc.*, in revision.
23 W. Liu, M. Howarth, A. B. Greytak, Y. Zheng, D. G. Nocera, A. Y. Ting and M. G. Bawendi, *J. Am. Chem. Soc.*, 2008, **130**, 1274–1284.
24 W. Liu, A. B. Greytak, J. Lee, C. R. Wong, J. Park, L. F. Marshall, W. Jiang, P. N. Curtin, A. Y. Ting, D. G. Nocera, D. Fukumura, R. K. Jain and M. G. Bawendi, *J. Am. Chem. Soc.*, 2010, **132**, 472–483.
25 K. Susumu, H. T. Uyeda, I. L. Medintz, T. Pons, J. B. Delehanty and H. Mattoussi, *J. Am. Chem. Soc.*, 2007, **129**, 13987–13996.
26 G. R. Fulmer, A. J. M. Miller, N. H. Sherden, H. E. Gottlieb, A. Nudelman, B. M. Stoltz, J. E. Bercaw and K. I. Goldberg, *Organometallics*, 2010, **29**, 2176–2179.
27 K. Rurack and M. Spieles, *Anal. Chem.*, 2011, **83**, 1232–1242.
28 M. Grabolle, M. Spieles, V. Lesnyak, N. Gaponik, A. Eychmüller and U. Resch-Genger, *Anal. Chem.*, 2009, **81**, 6285–6294.
29 A. A. Pizano, D. A. Lutterman, P. G. Holder, T. S. Teets, J. Stubbe and D. G. Nocera, *Proc. Natl. Acad. Sci. USA*, 2012, **109**, 39–43.
30 P. G. Holder, A. A. Pizano, B. L. Anderson, J. Stubbe and D. G. Nocera, *J. Am. Chem. Soc.*, 2012, **134**, 1172–1180.
31 Z. H. Loh, S. E. Miller, C. J. Chang, S. D. Carpenter and D. G. Nocera, *J. Phys. Chem. A*, 2002, **106**, 11700–11708.
32 J. R. Lakowicz, *Principles of Fluorescence Spectroscopy*, 3rd ed., Springer, 2006.
33 I. Z. Steinberg, *Annu. Rev. Biochem.*, 1971, **40**, 83–114.

34 F. C. Chen and S. J. Chen, *Opt. Lett.*, 2006, **31**, 187–189.
35 *CRC Handbook of Chemistry and Physics*, 84th ed., CRC Press, 2003.
36 A. Javier, D. Magana, T. Jennings and G. F. Strouse, *Appl. Phys. Lett.*, 2003, **83**, 1423–1425.
37 M. Jones, S. S. Lo and G. D. Scholes, *Proc. Natl. Acad. Sci. U.S.A.*, 2009, **106**, 3011–3016.
38 K. D. Bonin and T. J. McIlrath, *J. Opt. Soc. Am. B: Opt. Phys.*, 1984, **1**, 52–55.
39 S. A. Blanton, M. A. Hines, M. E. Schmidt and P. Guyot-Sionnest, *J. Lumin.*, 1996, **70**, 253–268.
40 B. Dubertret, P. Skourides, D. J. Norris, V. Noireaux, A. H. Brivanlou and A. Libchaber, *Science*, 2002, **298**, 1759–1762.
41 T. Ren, P. K. Mandal, W. Erker, Z. Liu, Y. Avlasevich, L. Puhl, K. Müllen and T. Basché, *J. Am. Chem. Soc.*, 2008, **130**, 17242–17243.
42 L. Dworak, V. V. Matylitsky, T. Ren, T. Basché and J. Wachtveitl, *J. Phys. Chem. C*, 2014, **118**, 4396–4402.
43 E. Zenkevich, F. Cichos, A. Shulga, E. P. Petrov, T. Blaudeck and C. von Borczyskowski, *J. Phys. Chem. B*, 2005, **109**, 8679–8692.
44 E. I. Zenkevich, E. I. Sagun, V. N. Knyukshto, A. S. Stasheuski, V. A. Galievsky, A. P. Stupak, T. Blaudeck and C. von Borczyskowski, *J. Phys. Chem. C*, 2011, **115**, 21535–21545.
45 C. M. Lemon and P. J. Brothers, *J. Porphyrins Phthalocyanines*, 2011, **15**, 809–834.